Acta Materialia 254 (2023) 119021

Contents lists available at ScienceDirect

Acta Materialia

journal homepage: www.elsevier.com/locate/actamat

Understanding the effect of microstructural texture on the anisotropic elastic properties of selective laser melted Ti-24Nb-4Zr-8Sn

Vivien J. Challis [a,b,*,1], Xiaoxue Xu [c,2], Angela Halfpenny [d,3], Andrew D. Cramer [a], Martin Saunders [e], Anthony P. Roberts [a,b,1], T.B. Sercombe [c]

[a] School of Mathematics and Physics, The University of Queensland, St Lucia, QLD 4072, Australia
[b] School of Mathematical Sciences, Queensland University of Technology, Brisbane, QLD 4001, Australia
[c] School of Engineering, The University of Western Australia, Perth, WA 6009, Australia
[d] CSIRO, Earth Science and Resource Engineering, Australian Resource Research Centre, Kensington, WA 6151, Australia
[e] Centre for Microscopy, Characterisation and Analysis, The University of Western Australia, Perth, WA 6009, Australia

ARTICLE INFO

Keywords:
Selective laser melting
Texture
Titanium alloys
Elastic properties
Computational homogenisation

ABSTRACT

Due to their low Young's Modulus, high strength and suitability for additive manufacturing, non-toxic beta-type titanium alloys are emerging as next-generation biomaterials. We present novel experimental results that demonstrate significant variation of Young's Modulus with direction for selective laser melted (SLM) biocompatible Ti-24Nb-4Zr-8Sn (Ti2448). Grain orientation data for SLM-processed Ti2448 is measured using electron backscatter diffraction. By assuming the grain orientations are fixed relative to the axes of the SLM build machine, the measured grain orientation data is used to generate a detailed microstructural finite element model of the polycrystalline SLM-processed material. The computational model provides excellent predictions of the anisotropic properties of SLM-processed Ti2448, indicating that preferential grain orientations that form during SLM processing of Ti2448 cause the experimentally measured variation of the Young's Modulus. The results show that computational models are able to accurately predict the anisotropic Young's Modulus of polycrystalline materials, and, in the context of biocompatible Ti2448 show how to tailor the modulus of SLM components by choosing the build orientation.

1. Introduction

The relatively low modulus of titanium, along with its excellent corrosion resistance and very high specific strength, has resulted in it being widely favoured in bone replacement applications [1]. Even so, Ti has a modulus which is at least an order of magnitude larger than bone. Mismatch of moduli between the biomaterial and surrounding bone can cause stress shielding in the bone, which eventually leads to bone resorption, and has been identified as a major causal factor of implant loosening [2,3]. Although commonly used titanium alloys (commercially pure Ti or Ti-6Al-4 V) have a much lower modulus than the more traditional stainless steel or Co-Cr alloys, they are still much stiffer than bone. As a result, a new generation of low-modulus beta titanium alloys have been developed that are comprised of non-toxic and non-allergic elements [4,5]. One such alloy, Ti-24Nb-4Zr-7.9Sn (Ti2448), has a modulus that is approximately half that of conventional titanium alloys combined with a strength between 800 and 1200 MPa [6–8]. The suitability of this alloy for Selective Laser Melting (SLM), one of the key emerging additive manufacturing technologies, has been demonstrated for both solid [9] and porous parts [10].

Due to the layer-by-layer processing method and directional heat flow, preferred grain orientations are often reported in SLM fabricated parts. For example, microstructural texture has been reported in selective laser melted aluminium [11–13], titanium [14–24], stainless steel [25–27], nickel [28–33] and tantalum [34] alloys. In Ti-6Al-4 V, the prior β grains have been shown to preferentially grow with the [001] parallel to the build direction [16–18]. This led to a directional solidification structure and thus anisotropy of the properties [16]. In SLM

* Corresponding author.
E-mail address: vivien.challis@qut.edu.au (V.J. Challis).
[1] Present address: School of Mathematical Sciences, Queensland University of Technology, 2 George Street, Brisbane, QLD 4001, Australia.
[2] Present address: Institute for Biomedical Materials and Devices, Faculty of Science, University of Technology Sydney, Sydney, NSW 2007, Australia.
[3] Present address: Stanford Doerr School of Sustainability, Stanford University, 397 Panama Mall, Stanford, CA, 94,305, USA.

https://doi.org/10.1016/j.actamat.2023.119021
Received 15 May 2022; Received in revised form 17 April 2023; Accepted 15 May 2023
Available online 16 May 2023

fabricated Ti2448, anisotropy of tensile strength and plasticity has been reported, along with superior properties compared to the forged alloy [35]. The β-phase of Ti2448 has a particularly anisotropic stiffness, with the [100], [110] and [111] orientated crystals having Young's Moduli of 27.1, 56.3 and 88.1 GPa, respectively [36].

Several recent works have used computational modelling to understand how texture arises in the SLM process [37–39]. Furthermore, the effect of different scanning strategies on texture has been studied [27, 32]. Texture in SLM stainless steel can be controlled by switching scanning strategies for different portions of the component [27]. Moreover, use of a secondary laser heat source has been suggested as a way to control the grain structure and achieve a more uniform texture in SLM Ti-6Al-4 V [40]. However, we note that none of these works have used theoretical or computational tools to predict how the modelled or observed texture affects mechanical properties.

There is a long history of research that has used theoretical and computational homogenisation to explore how the microstructure of an inhomogeneous material affects its macroscopic properties (see, e.g., [41]). The polycrystalline nature of SLM fabricated Ti2448, where each grain within the material has its own orientation and subsequent anisotropic material properties, lends itself towards a computational rather than theoretical homogenisation approach, and it is important to have an accurate representation of the polycrystalline microstructure [42]. Both finite element and fast Fourier transform (FFT)-based methods have been used successfully in the context of polycrystalline materials to determine macroscopic properties, including for complex phenomena such as crystal plasticity and fatigue (see, e.g., [42]).

In this paper we utilise both experimental and computational approaches to advance our understanding of the texture and anisotropic elastic properties of SLM processed Ti2448. By assuming that the grain orientations are fixed relative to the axes of the SLM build machine, we generate a detailed finite element model of SLM Ti2448 using experimentally measured grain orientations data and knowledge of the SLM build process. We also manufacture Ti2448 SLM samples in different orientations to measure the directional variation of the Young's Modulus. The computational model is used to predict the elastic properties from the observed grain orientations and these are compared to the experimental measurements. Finally, instead of aiming to minimise the effect of the microstructural texture, we use our FE model to predict in which direction Ti2448 parts should be built to achieve the lowest possible Young's Modulus.

The remainder of this paper is as follows. Our experimental methods and results are presented in Sections 2 and 3. We then present our computational methods and results in Sections 4 and 5. The results are discussed in Section 6, and concluding remarks are presented in Section 7.

2. Experimental materials and methods

2.1. SLM processing of Ti2448

The Ti2448 powder used in this study was electrode induction gas atomised (EIGA) by TLS Technik Germany from an ingot fabricated via vacuum arc melting [6]. Selected properties of the powder are summarised in Table 1. The chemical composition was measured by inductively coupled plasma atomic emission spectroscopy (ICP-AES) by Spectrometer Services (Melbourne, Australia) and the O and N content determined using a Leco O/N analyser (Spectrometer Services, Melbourne). The particle size was measured using a Malven Microsizer Plus and the powder flow and apparent density were measured according to ASTM B964 and B212–13 respectively. The theoretical density of the alloy was taken to be the density of the solid ingot, 5.42 g/cm^3, which was presumed to be fully dense.

SLM was performed on a Realizer SLM 100 (Borchen, Germany) using a fibre laser (λ=1.06 μm) with a maximum power of 200 W. The laser scanning strategy was to first trace the outline of the part and then fill with a series of parallel vectors. The orientation of the fill vectors alternated between layers and was parallel to the X or Y axis of the machine. Specifically, the pattern of fill vectors was aligned along the X axis for one layer, the Y axis for the next layer, and continued to alternate between layers.

The SLM laser power, scan spacing, and layer thickness were kept constant at 175 W, 120 μm and 50 μm, respectively, while the laser scan speed was varied between 625 and 2000 mm/s. Initially, 10 mm × 10 mm × 10 mm cubes were built and their densities measured using Archimedes' principle following Metal Powder Industries Federation Standard 42. The highest density was attained at a laser scan speed of 1000 mm/s and was 98.9 ± 0.2%. At speeds greater than 1000 mm/s the density decreased linearly with increasing speed as a result of insufficient energy to completely melt all the particles [9]. For speeds slower than the optimum the excess energy caused balling and dross formation in the melt pool, which led to poor surface finish and lower density [9, 43]. All subsequent SLM builds for this paper use a laser scan speed of 1000 mm/s.

2.2. Measurement of directional Young's Modulus

SLM-produced Ti-2448 cylinders 10 mm in diameter and 60 mm long were produced in several different orientations. We use a nomenclature similar to crystallography to indicate orientation, with [100] representing a sample aligned to the X-axis and [111] representing a sample aligned between the coordinates (0,0,0) and (1,1,1). In this study we fabricated 28 cylinders with the orientations [100], [010], [001], [110], [101], [011], and [111], as illustrated in Fig. 1 (four samples for each orientation). The as-printed samples were machined into cylinders 8 mm diameter and 58 mm long to remove effects related to being near the edge of the SLM sample.

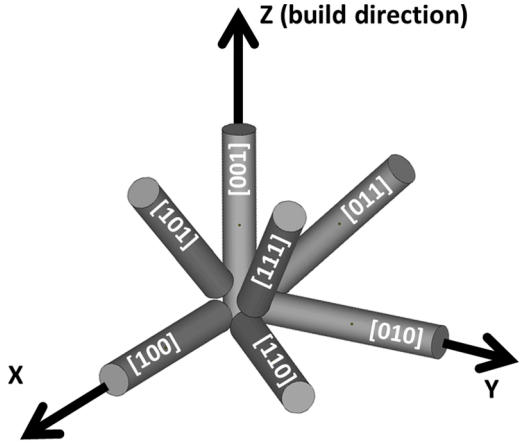

Fig. 1. Ti2448 cylinders were built using SLM in the orientations shown to allow measurement of the directional Young's Modulus.

Table 1
Properties of the Ti2448 powder used in this study.

Powder Composition (wt%)						Powder Size (μm)			Flow Rate (s/50 g)	Apparent Density (%)
Ti	Nb	Zr	Sn	O	N	d_{10}	d_{50}	d_{90}	20.5	53.3
Bal	23.2	3.85	8.1	0.15	<0.005	42.6	69.2	106.1		

The Young's Modulus of the SLM-produced cylinders was measured using a non-destructive impulse excitation technique (IMCE, Belgium). Each cylinder was placed on supports positioned at the nodes of the flexural mode and subsequently tapped on its end to induce a flexural vibration. Dedicated software then computed the Young's Modulus along the length of the sample using the measured frequency of the flexural vibration along with the length, diameter and mass of the sample. Additionally, the density of each bar was measured using Achimedes's principle following Metal Powder Industries Federation Standard 42.

2.3. Measurement of grain orientations

Grain orientations of SLM-processed Ti-2448 were measured as follows. As-produced 10 mm × 10 mm × 10 mm cubes were chemically-mechanically polished for 2 h using a Buehler VibroMet 1 fitted with a Buehler ChemoMet pad and using Buehler MasterMet colloidal silica polishing suspension [44,45]. The samples were then analysed via electron backscatter diffraction (EBSD) to measure the full crystallographic orientation of the grains.

The data were obtained from automatically indexed Kikuchi diffraction patterns collected using a Bruker e^-Flash detector on a Zeiss Ultraplus FEG SEM at the CSIRO facilities, Kensington, Western Australia. The SEM was operated using an accelerating voltage of 20 kV, a 120 μm aperture, in high current mode which produced a beam current of 12.1 nA. The EBSD data were collected using the Bruker Quantax Espirit 1.9 software, using an EBSP resolution of 160 × 120 pixels, 8 ms exposure time and a step size between measurements of 2.2 μm. If the pattern quality was poor and the software was unable to find the correct crystallographic solution, then the point was not indexed. Non-indexed points are common in areas of poor surface quality, on grain boundaries, cracks and where the surface is contaminated. The EBSD data were post-processed using Oxford Instruments Channel 5 software to remove mis-indexed points and interpolate non-indexed points. The EBSD data were also post-processed to ensure alignment of visible scan tracks with the X axis.

The open-source software MTEX [46] was used to estimate the orientation distribution function of a layer of additively manufactured Ti2448 from the measured EBSD data using a kernel half-width of 4°. Pole figures were then generated from the estimated orientation distribution function.

3. Experimental results

3.1. Young's Modulus and density data

The experimentally measured Young's Modulus for SLM Ti2448 cylinders built in different orientations is presented in Fig. 2. As expected, it is clear that build orientation has a significant effect on the Young's Modulus of SLM manufactured Ti2448. Due to the alternating X-Y scanning strategy, the X and Y directions are equivalent and expected to demonstrate a different Young's Modulus to that of the Z direction, which is the build direction of the SLM machine. More specifically, the thermal conditions experienced in the [100] (X-) direction are identical to the [010] (Y-) direction. Similarly, the [101] direction is equivalent to the [011] direction, which are both different to [110]. The presented data in Fig. 2 is consistent with this. It is clear that the [110] direction has the highest modulus, followed by the [001] and [111] directions which are similar. The lowest modulus values are obtained for samples aligned to the [100]/[010] and [101]/[011] directions. Regardless of the direction, the modulus of the SLM produced material is higher than that of wrought Ti2448, which has been reported to be between 42 and 52 GPa depending on composition and processing [47–49].

Figure 3 shows the measured density of the SLM fabricated Ti2448 cylinders for the different build orientations. Although there is an approximately ±0.5% scatter in the data, there is little or no dependence of density on orientation. Further, extracting out the data for the stiffest ([110]) and most compliant directions ([100] and [010]), Fig. 4 clearly shows that it is not density that is the causal factor of the orientation dependence of the Young's Modulus.

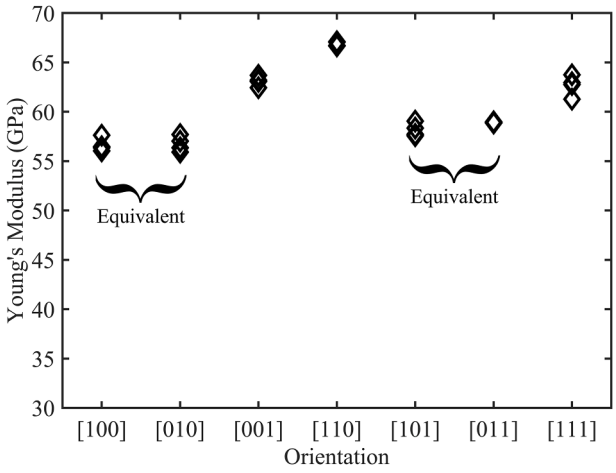

Fig. 2. Experimentally measured Young's Modulus values for SLM-processed Ti2448 cylinders with the orientations shown in Fig. 1. There are four experimental measurements for each orientation.

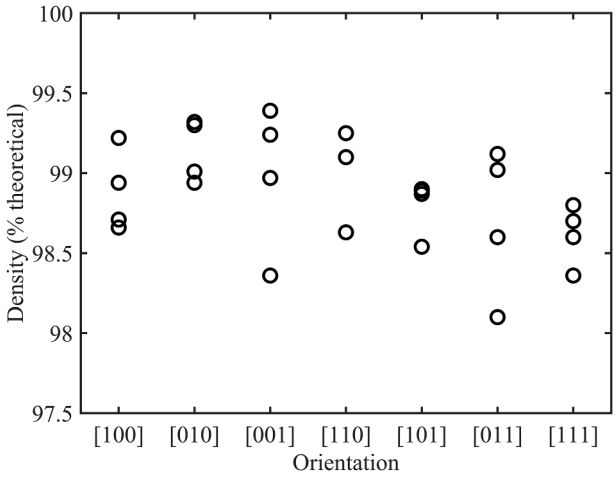

Fig. 3. The density of the individual SLM produced samples as a function of build direction. There is no obvious trend in this data.

3.2. EBSD grain orientation data

The post-processed EBSD grain orientation measurements for a single layer of SLM fabricated Ti2448 are presented in Fig. 5. The laser scan tracks are visible within the measured data. Under the assumption that grain orientations are fixed relative to the axes of the SLM build machine, the EBSD data presented in Fig. 5 enables us to generate a detailed microstructural model of polycrystalline SLM-processed Ti2448 material.

In Fig. 6 we present pole figures of the estimated orientation distribution function generated from the EBSD data in Fig. 5. The pole figures show a weak crystallographic texture, with no strongly preferred orientations. The pole figures are useful in understanding the experimentally measured Young's Moduli for SLM Ti2448 cylinders built in different orientations as presented in Fig. 2. For example, the pole figure for [100] indicates a lower than uniform density of [100] poles aligned along the Z axis. Ti2448 crystals have a low Young's Modulus in

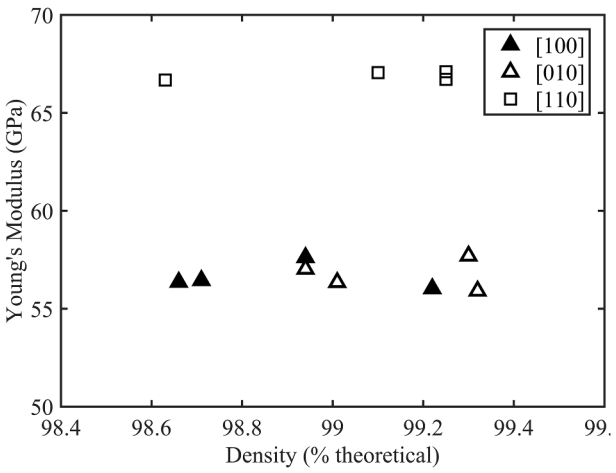

Fig. 4. The effect of density on the experimentally determined Young's Modulus of individual samples for the [100], [010] and [110] directions. Clearly the difference in density of the individual samples does not account for the variation in the Young's Modulus.

direction [100] [36], so this pole figure explains the higher Young's Modulus measured experimentally for additively manufactured Ti2448 cylinders built in orientation [001] compared to [100] and [010].

4. Computational methods

In this section we outline the computational approach used to model the elastic properties of polycrystalline SLM-processed Ti2448. We note that the computational homogenisation approach is relatively standard (see, e.g., [42,50]), and the novelty lies in the development of the model from our knowledge of the SLM build process combined with experimentally measured grain orientations data. This approach enables us to appropriately ascribe anisotropic elastic properties to each element of the model.

4.1. Generation of finite element model from EBSD data

A finite element (FE) model of SLM-processed Ti2448 was constructed using the EBSD data. A block of SLM-processed Ti2448 440 μm × 440 μm × 440 μm in size was modelled using a representative volume element (RVE) of 200 × 200 × 200 hexahedral (i.e., cube) elements.

Figure 7 illustrates the construction of an RVE from the grain orientations data in Fig. 5. The 200 × 200 × 200 element cube was separated into 8 layers. Each layer was 25 elements thick. This layer thickness corresponds to 55 μm, which approximately matches the thickness of a single layer of the SLM build. Grain orientations within each layer were prescribed using a randomly chosen 440 μm × 440 μm portion of EBSD data. For every second layer the grain positions and orientations were rotated by 90° about the Z axis to account for the alternating fill vectors in the layers of the SLM build process. Four RVEs were generated with the above process to enable an understanding of the possible variation in the elastic properties of SLM-processed Ti2448.

Elastic properties for each element within each RVE were prescribed using the orientation in terms of Euler angles of the Ti2448 grains from the EBSD data and the known elastic properties of Ti2448 single crystals [36]. We aligned the X axis with the visible scan tracks in the experimental data. The Bunge convention for the Euler angles was used [51], where crystal orientation is defined using a rotation through angle φ_1 about the Z axis, followed by a rotation through angle Φ about the X axis in its new orientation X', finally followed by a rotation through angle φ_2 about the Z axis in its new orientation Z'. The adjustment of the Euler angles for every second layer of the RVE to account for alternating fill-vectors was implemented by incrementing the value of φ_1 for these elements by 90°.

As noted above in Section 3.1, the Young's Modulus measurements for our SLM processed Ti2448 are higher than that of wrought Ti2448. We therefore introduce a calibration factor into our computational model that will account for the SLM processed Ti2448 having higher Young's Modulus than Ti2448 single crystal data. In doing so, we are assuming that the crystals within SLM processed Ti2448 have the same anisotropic body-centred cubic (BCC) crystal structure as Ti2448 single crystal specimens, but we are adjusting the stiffness of the base material to reflect the higher stiffness of the SLM processed alloy. We therefore write the base elasticity tensor of SLM processed Ti2448 for Euler angles $\{\varphi_1,\ \Phi, \varphi_2\} = \{0, 0, 0\}$ in Voigt notation as [41]

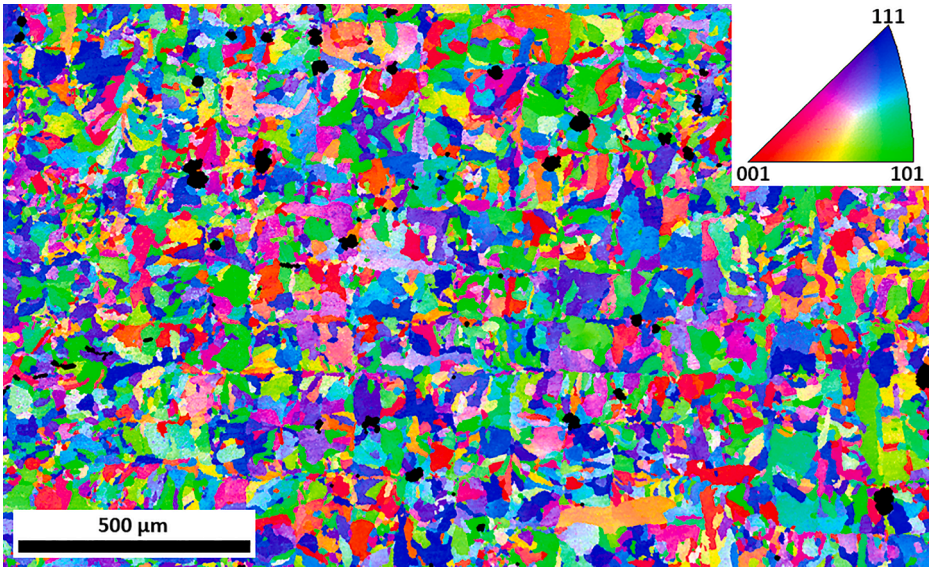

Fig. 5. Inverse Pole Figure colouring of the electron backscatter diffraction (EBSD) data. The orientation is measured parallel to the Z axis. This data relates to a single layer of the SLM build, from a horizontal slice of an as-processed sample of Ti2448.

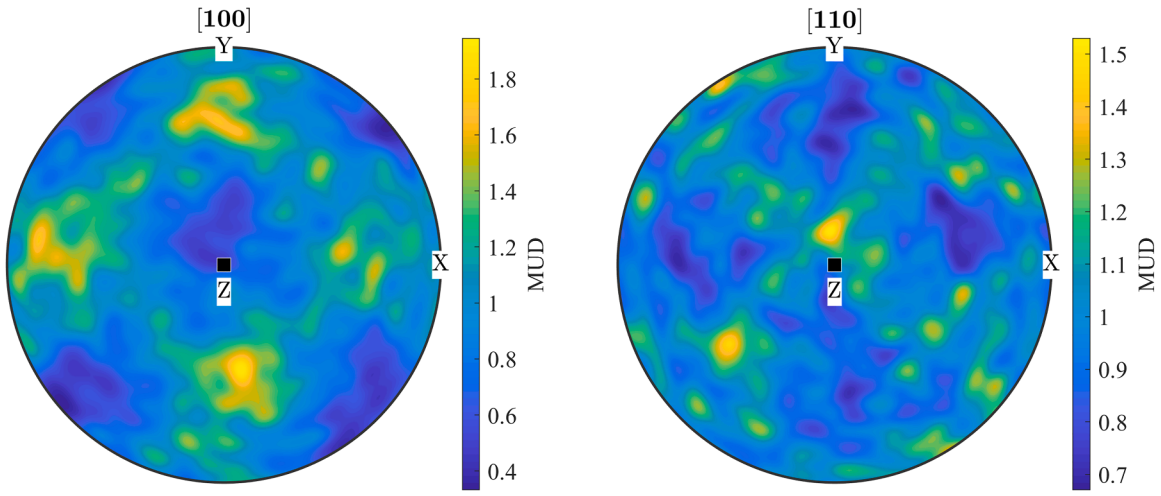

Fig. 6. Pole figures for a layer of additively manufactured Ti2448 generated from the EBSD data presented in Fig. 5. The colour indicates multiples of uniform density (MUD).

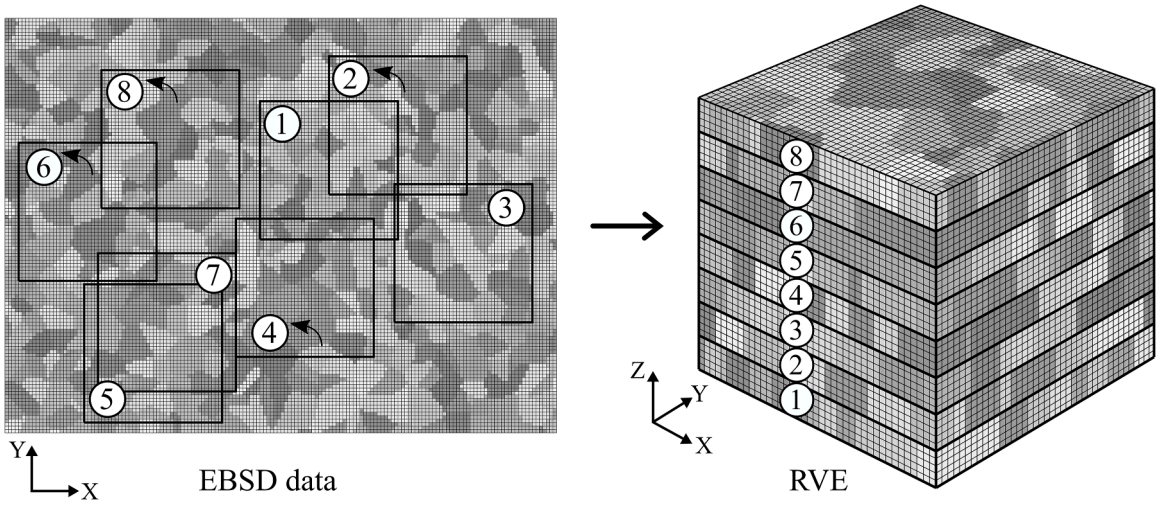

Fig. 7. A schematic explaining how a representative volume element (RVE) for SLM-processed Ti2448 is constructed from the EBSD grain orientation data. Eight randomly chosen square portions of the EBSD data are layered into the RVE. As indicated by the curved arrows, every second layer (2, 4, 6 and 8) is rotated by 90° A single cube element in the depicted RVE on the right represents 5 × 5 × 5 elements in the computational model.

$$\left[C^0_{\alpha\beta}\right] = C \times \begin{bmatrix} C_{11} & C_{12} & C_{12} & 0 & 0 & 0 \\ C_{12} & C_{11} & C_{12} & 0 & 0 & 0 \\ C_{12} & C_{12} & C_{11} & 0 & 0 & 0 \\ 0 & 0 & 0 & C_{44} & 0 & 0 \\ 0 & 0 & 0 & 0 & C_{44} & 0 \\ 0 & 0 & 0 & 0 & 0 & C_{44} \end{bmatrix}$$

where using Ti2448 single crystal data we prescribe $C_{11} = 57.2$ GPa, $C_{12} = 36.1$ GPa and $C_{44} = 35.9$ GPa [36], and the factor C accounts for the SLM processed alloy having a higher base stiffness. We expect that the factor C is slightly larger than unity. Due to linearity, we performed the following calculations with $C = 1$. The appropriate value of C was then determined via a comparison of the computational and experimental Young's Modulus data using a least-squares error minimisation approach.

We subsequently prescribe the elasticity tensor C_{ijkl} for a finite element with Euler angles $\{\varphi_1,\ \Phi, \varphi_2\}$ as

$$C_{ijkl}(\varphi_1,\ \Phi, \varphi_2) = R_{pi}R_{qj}R_{rk}R_{sl}C^0_{pqrs},$$

where C^0_{pqrs} is the above base elasticity tensor for Ti2448 in index notation (equivalent to $[C^0_{\alpha\beta}]$ in Voigt notation), and summation is implied on the repeated indices $p,\ q,\ r$ and s that each range from 1 to 3. The rotation matrix $R_{ij} \equiv [R(\varphi_1,\ \Phi, \varphi_2)]$ is given by [51]

$$[R(\varphi_1,\ \Phi, \varphi_2)] = \left[g^{Z'}_{\varphi_2}\right] \cdot \left[g^{X'}_{\Phi}\right] \cdot \left[g^{Z}_{\varphi_1}\right]$$

where $[g^W_\theta]$ is the rotation matrix for rotation about axis W by angle θ.

4.2. Computational homogenisation

Computational homogenisation [50,52,53] was used to calculate effective elastic properties of each RVE. The state equations for linear elasticity over an RVE Ω under an applied macroscopic strain $\bar{\epsilon}_{ij}$ can be written as [50]

$$\begin{aligned} \sigma_{ij,i} &= 0 \\ \sigma_{ij} &= C_{ijkl}(\varphi_1, \Phi, \varphi_2)\epsilon_{kl} \\ \epsilon_{ij} &= \frac{1}{2}\left(u_{i,j} + u_{j,i}\right) \\ \frac{1}{\mathrm{Vol}(\Omega)} \int\int\int_{\Omega} \epsilon_{ij}\, \mathrm{d}\Omega &= \bar{\epsilon}_{ij} \end{aligned}$$

where σ_{ij} is the stress tensor, ϵ_{ij} is the strain tensor that must be Ω-periodic, u_i is the displacement field and Vol(Ω) is the volume of Ω. Note that the elasticity tensor in the constitutive law that relates stresses to strains depends on the three Euler angles, and thus varies within each RVE. Summation is implied on repeated indices and the comma notation is used for spatial derivatives. These state equations are solved with the finite element method for the six applied strain fields given by

$$\overline{\epsilon}_{ij}^{(kl)} = \frac{1}{2}\left(\delta_{ik}\delta_{jl} + \delta_{il}\delta_{jk}\right).$$

The effective elasticity tensor of the RVE Ω is then given by [41,50]

$$\overline{C}_{ijkl} = \int_{\Omega}\int\int C_{pqkl}(\varphi_1,\ \Phi, \varphi_2)\epsilon_{pq}^{(ij)}\mathrm{d}\Omega$$

where summation is implied on repeated indices and $\epsilon_{pq}^{(ij)}$ is the strain field resulting from the applied macroscopic strain $\overline{\epsilon}_{kl}^{(ij)}$.

4.3. Calculation of Young's Modulus

Effective elasticity tensors $\overline{C}_{ijkl}$ were calculated for the four RVEs generated from the EBSD data. To allow comparison with the experimental data, for each RVE the Young's Modulus was calculated for each of the orientations in Fig. 1. The effective Young's Modulus $\overline{E}_{\boldsymbol{n}}$ in the direction of a unit vector $\boldsymbol{n}$ can be calculated via

$$\overline{E}_{\boldsymbol{n}} = \frac{1}{\overline{S}_{ijkl}n_i n_j n_k n_l}$$

where summation is implied on repeated indices and $\overline{S}_{ijkl}$ is the effective compliance tensor. The effective compliance tensor is the inverse of the effective elasticity tensor $\overline{C}_{ijkl}$.

To determine the direction $\boldsymbol{n}$ that would give the minimum Young's Modulus, we averaged the effective elasticity tensor $\overline{C}_{ijkl}$ over the four RVEs and subsequently performed a minimisation of the effective Young's Modulus $\overline{E}_{\boldsymbol{n}}$ over the possible directions $\boldsymbol{n}$. The minimisation was performed using Matlab's `fmincon` function (Mathworks).

5. Computational results

We computed the effective Young's Modulus of four RVEs constructed using Euler angles from the experimental EBSD data. This enabled us to determine the appropriate scale factor C of 1.123 to account for the higher stiffness of the SLM-processed Ti2448 material. This factor adjusts our estimate of the Young's Modulus of SLM processed Ti2448 crystals to be approximately 30, 63 and 99 GPa in the [100], [110] and [111] directions, respectively, rather than the values of 27.1, 56.3 and 88.1 GPa measured for Ti2448 single crystals grown using an optical floating-zone furnace [36]. The estimated Young's Modulus of the SLM processed BCC Ti2448 crystals is visualised in the left of Fig. 8 (c.f. Fig. 3(a) of [36]), which clearly demonstrates the anisotropy of the Ti2448 grains.

The computed effective Young's Modulus of the SLM processed Ti2448 is visualised in the right of Fig. 8. We note that the elastic properties of four RVEs generated from the EBSD data have been averaged to obtain a single visualisation. The non-spherical nature of the visualisation shows that the FE model predicts significant variation of the Young's Modulus with direction for SLM processed Ti2448. This asymmetry arises from the combination of microstructural texture and the very different modulus of the BCC Ti2448 crystals in the [100], [110] and [111] directions (as shown in the left of Fig. 8).

Figure 9 shows a comparison of the computationally predicted Young's Modulus with the experimentally measured values for the orientations in Fig. 1. We see an excellent match between the computational predictions and the experimental measurements. We emphasise that the computationally predicted Young's Modulus along direction [100] is approximately equivalent to that along direction [010], and similarly for directions [101] and [011], which reflects the symmetries present in the SLM Ti2448 material.

Computational optimisation using the FE data displayed in the right of Fig. 8 predicts a minimum Young's Modulus along the direction vector (−0.03, 0.92, 0.40). This direction is calculated to have a Young's Modulus of 49.6 GPa. As an additional validation of our computational model, four cylinders of Ti2448 were fabricated in this calculated direction of minimum Young's Modulus. The cylinders were fabricated with SLM as described in Sections 2.1 and 2.2. A Young's Modulus of 49.9 ± 0.4 GPa was measured for these samples, which is in excellent agreement with the computational prediction of 49.6 GPa.

6. Discussion

The experimental data presented in Fig. 2 clearly show that build orientation has a significant effect on the Young's Modulus of SLM

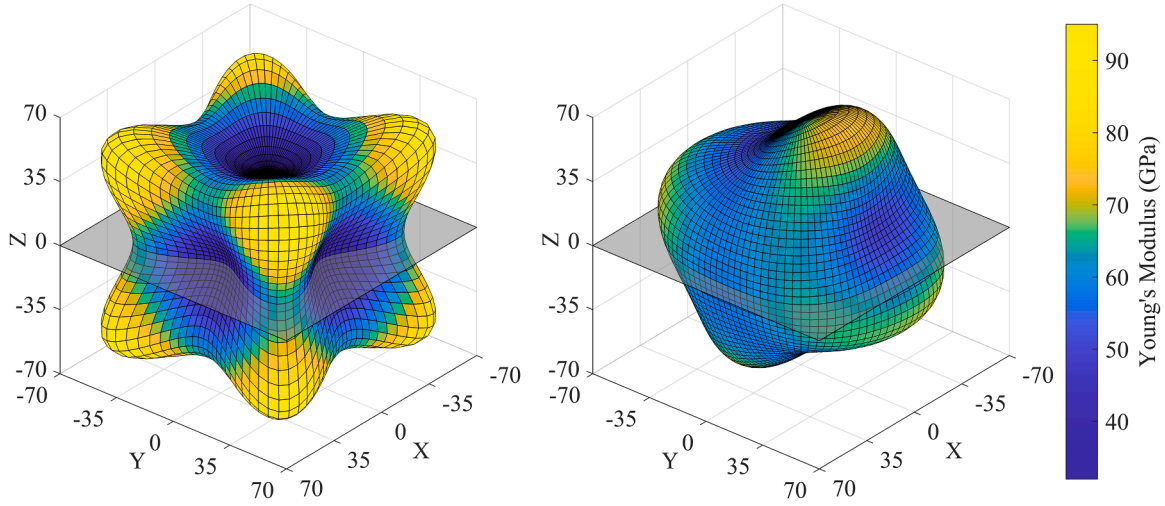

Fig. 8. Estimated Young's Modulus of a single SLM BCC Ti2448 grain with Euler angles of $\{\varphi_1,\ \Phi, \varphi_2\} = \{0, 0, 0\}$ (left) and calculated Young's Modulus of SLM manufactured Ti2448 (right), with the XY-plane shown for clarity. At a point on each surface, the distance to the origin is the Young's Modulus along the direction to the origin. The asymmetrical shape on the right indicates that SLM processed Ti2448 is anisotropic. This results from the directional Young's Modulus variation of the BCC Ti2448 grains (as shown on left) and microstructural texture.

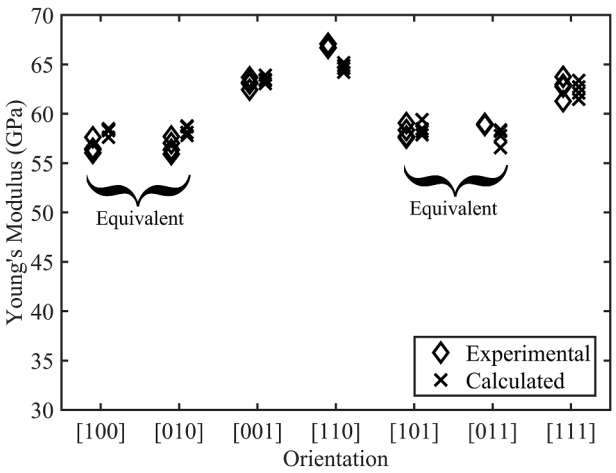

Fig. 9. A comparison of the experimentally measured and computationally calculated Young's Modulus values for the directions shown in Fig. 1. The four calculated data points for each orientation correspond to the four different RVEs generated from the EBSD data. As indicated, symmetries present in the SLM material are also reflected in the calculated Young's Modulus values.

manufactured Ti2448. The density data presented in Fig. 4 demonstrates that variation in density of the SLM-processed samples is not responsible for the measured directional variation of the Young's Modulus. Instead, our hypothesis is that preferred grain orientations that form during the SLM process cause the observed variation of the Young's Modulus.

Ti2448 is a metastable β titanium alloy with a BCC unit cell. Like most BCC materials, the Young's Modulus of Ti2448 varies significantly according to the crystallographic orientation of the unit cell. The Young's Modulus of Ti2448 single crystals grown using an optical floating-zone furnace has been measured to be 27.1, 56.3 and 88.1 GPa in the [100], [110] and [111] directions, respectively [36]. Hence, changes in the preferred orientation of polycrystalline materials (i.e., texture) are likely to result in changes in Young's Modulus. The laser scanning vectors in the SLM build process are defined relative to the axes of the SLM machine, therefore the texture or preferred orientation of the Ti2448 grains is also likely to be fixed relative to the build axes of the machine. The orientation of the Ti2448 grains will therefore vary relative to the sample if a sample is built in different orientations.

The pole figures presented in Fig. 6 and generated from the EBSD data in Fig. 5 show a relatively weak crystallographic texture within SLM-processed Ti2448. Nevertheless, there are clear variations in the estimated orientation distribution function that contribute to the anisotropic Young's Modulus properties of SLM Ti2448. The relatively weak crystallographic texture explains why the variation in Young's Modulus for the SLM-processed material is much less significant than the variation that occurs for Ti2448 BCC single crystals (see Fig. 8). The pole figures provide additional validation and understanding of the variation in Young's Modulus measured experimentally and predicted by the FE model.

Our FE model of the polycrystalline SLM-processed Ti2448 assumes that microstructural texture is fixed relative to the axes of the SLM build machine and predicts directional variation of the Young's Modulus in very good agreement with our experimental measurements. Therefore, our work strongly suggests that the preferred orientation of the Ti2448 crystals relative to the axes of the build machine causes the experimentally observed directional variation in Young's Modulus. We emphasise that our calculated values are computed directly from the measured EBSD data by generating a novel FE model of SLM-processed Ti2448. The properties of each element within the model are prescribed using the Euler angles from the EBSD data and modulus data from Ti2448 single crystals [36] with a scale factor to account for the stiffness of the SLM processed alloy being significantly higher than its notional value. The calculated scale factor of 1.123 indicates that the Ti2448 single crystals within the SLM-processed material have Young's Moduli of approximately 30, 63 and 99 GPa in the [100], [110] and [111] directions, respectively. Such a high measured stiffness may have occurred because the composition of the alloy was not quite correct, see Table 1. In particular, the Nb content at 23.2% was lower than target 24%, which would increase the modulus of the material by ~10% [47]. This would account for most of the difference observed. In addition to this, SLM processing tends to increase the oxygen content by ~0.05%, which tends to increase the modulus [9].

As one further test of our computational model, we computationally predicted the direction and value of the minimum Young's Modulus. The measured Young's Modulus of 49.9 ± 0.4 GPa for the samples built along the predicted minimum Young's Modulus direction (−0.03, 0.92, 0.40) matched well with the computationally predicted value of 49.6 GPa. Moreover, this demonstrates an important capability facilitated by the computational analysis in this paper: that of being able to tailor the Young's Modulus of an SLM sample by choosing the build orientation. Our calculations indicate that by altering the build direction alone, it is possible to adjust the Young's Modulus of SLM-produced Ti2448 between approximately 50 and 70 GPa. This is significant new knowledge relevant to the production of Ti2448 parts and with broader relevance to selective laser melting of other alloys.

7. Conclusion

In this paper we have presented experimentally measured Young's Modulus and crystallographic texture data for SLM-processed Ti2448. We have shown that the directional Young's Modulus of a Ti2448 sample produced with SLM can be predicted with high accuracy using a detailed finite element model of the SLM-processed polycrystalline material. Our model was developed using EBSD grain orientation data; knowledge of the anisotropic properties of Ti2448 single crystals; an understanding of the layered nature of the SLM build process; and the assumption that the grain orientations are fixed relative to the axes of the SLM build machine. The computational Young's Modulus predictions accurately matched the anisotropic Young's Modulus variation of SLM-processed Ti2448 samples built in 7 different orientations. This work provides a strong demonstration that advanced computational methods coupled with accurate microstructural models can quantitatively predict the complex elastic properties of polycrystalline materials, including those additively manufactured.

In addition to success of the finite element method in accurately predicting the anisotropic elastic properties of the polycrystalline layered material, the method provided two further important outcomes in the context of additive manufacturing. First, the method enabled an estimate of the Young's Moduli of the Ti2448 crystals produced using SLM (which is 12.3% higher than the reference material). Second, our method shows how build orientation could be optimised to tailor the properties of SLM materials. In the case of Ti2448, our modelling accurately predicted a ~10%−25% reduction in the Young's Modulus of the SLM-processed material when built in the optimal orientation, compared to the orientations already considered. This reduction was realised experimentally and could potentially reduce stress shielding and the risk of implant loosening in implant applications.

Data availability statement

The data that support the findings of this study are available from the corresponding author upon reasonable request.

Declaration of Competing Interest

The authors declare that they have no known competing financial interests or personal relationships that could have appeared to influence the work reported in this paper.

Acknowledgments

This work was financially supported by the Australian Research Council (grant numbers DP110101653, LE110100094). This support is gratefully acknowledged. The first author thanks Dr C.J. Foster for assistance with generating Fig. 7. The authors also thank the anonymous reviewers for their suggestions that resulted in significant improvements to the manuscript.

References

[1] K. Wang, The use of titanium for medical applications in the USA, Mater. Sci. Eng. A 213 (1996) 134–137.
[2] W.C. Head, D.J. Bauk, R.H.J. Emerson, Titanium as the material of choice for cementless femoral components in total hip arthroplasty, Clin. Orthop. Relat. Res. 311 (1995) 85–90.
[3] D.M. Robertson, L. Peierre, R. Chahal, Preliminary observations of bone ingrowth into porous materials, J. Biomed. Mater. Res. 10 (1976) 335–344.
[4] M. Niinomi, Recent metallic materials for biomedical applications, Metal. Mater. Trans. A 33 (2002) 477–486.
[5] M. Geetha, A.K. Singh, R. Asokamani, A.K. Gogia, Ti based biomaterials, the ultimate choice for orthopaedic implants - a review, Prog. Mater. Sci. 54 (2009) 397–425.
[6] Y.L. Hao, S.J. Li, S.Y. Sun, C.Y. Zheng, Q.M. Hu, R. Yang, Super-elastic titanium alloy with unstable plastic deformation, Appl. Phys. Lett. 87 (2005), 091906.
[7] S.J. Li, T.C. Cui, Y.L. Hao, R. Yang, Fatigue properties of a metastable beta-type titanium alloy with reversible phase transformation, Acta Biomater. 4 (2008) 305–317.
[8] S.J. Li, Y.W. Zhang, B.B. Sun, Y.L. Hao, R. Yang, Thermal stability and mechanical properties of nanostructured Ti-24Nb-4Zr-7.9Sn alloy, Mater. Sci. Eng. A 480 (2008) 101–108.
[9] L.C. Zhang, D. Klemm, J. Eckert, Y.L. Hao, T.B. Sercombe, Manufacture by selective laser melting and mechanical behavior of a biomedical Ti-24Nb-4Zr-8Sn alloy, Scr. Mater. 65 (2011) 21–24.
[10] Y.J. Liu, S.J. Li, H.L. Wang, W.T. Hou, Y.L. Hao, R. Yang, Microstructure, defects and mechanical behavior of beta-type titanium porous structures manufactured by electron beam melting and selective laser melting, Acta Mater. 113 (2016) 56–67.
[11] L. Thijs, K. Kempen, J.-.P. Kruth, J. Van Humbeeck, Fine-structured aluminium products with controllable texture by selective laser melting of pre-alloyed AlSi10Mg powder, Acta Mater. 61 (2013) 1809–1819.
[12] K.G. Prashanth, S. Scudino, H.J. Klauss, K.B. Surreddi, L. Löber, Z. Wang, Microstructure and mechanical properties of Al–12Si produced by selective laser melting: effect of heat treatment, Mater. Sci. Eng. A 590 (2014) 153–160.
[13] L. Xi, P. Wang, K.G. Prashanth, H. Li, H.V. Prykhodko, S. Scudino, Effect of TiB2 particles on microstructure and crystallographic texture of Al-12Si fabricated by selective laser melting, J. Alloys Compd. 786 (2019) 551–556.
[14] A.A. Antonysamy, J. Meyer, P.B. Prangnell, Effect of build geometry on the β-grain structure and texture in additive manufacture of Ti6Al4V by selective electron beam melting, Mater. Charact. 84 (2013) 153–168.
[15] B. Vrancken, L. Thijs, J.P. Kruth, J. Van Humbeeck, Microstructure and mechanical properties of a novel β titanium metallic composite by selective laser melting, Acta Mater. 68 (2014) 150–158.
[16] S.S. Al-Bermani, M.L. Blackmore, W. Zhang, I. Todd, The origin of microstructural diversity, texture, and mechanical properties in electron beam melted Ti-6Al-4V, Metal. Mater. Trans. A 41 (2010) 3422–3434.
[17] B. Baufeld, O. Van der Biest, S. Dillien, Texture and crystal orientation in Ti-6Al-4V builds fabricated by shaped metal deposition, Metal. Mater. Trans. A 41 (2010) 1917–1927.
[18] X. Wu, J. Liang, J. Mei, C. Mitchell, P.S. Goodwin, W. Voice, Microstructures of laser-deposited Ti–6Al–4V, Mater. Des. 25 (2004) 137–144.
[19] T. Ishimoto, K. Hagihara, K. Hisamoto, S.-.H. Sun, T. Nakano, Crystallographic texture control of beta-type Ti–15Mo–5Zr–3Al alloy by selective laser melting for the development of novel implants with a biocompatible low Young's modulus, Scr. Mater. 132 (2017) 34–38.
[20] N. Kang, H. Yuan, P. Coddet, Z. Ren, C. Bernage, H. Liao, On the texture, phase and tensile properties of commercially pure Ti produced via selective laser melting assisted by static magnetic field, Mater. Sci. Eng. C 70 (2017) 405–407.
[21] C.-.L. Li, J.W. Won, S.-.W. Choi, J.-.H. Choe, S. Lee, C.H. Park, Simultaneous achievement of equiaxed grain structure and weak texture in pure titanium via selective laser melting and subsequent heat treatment, J. Alloys Compd. 803 (2019) 407–412.
[22] W. Li, J. Liu, S. Wen, Q. Wei, C. Yan, Y. Shi, Crystal orientation, crystallographic texture and phase evolution in the Ti–45Al–2Cr–5Nb alloy processed by selective laser melting, Mater. Charact. 113 (2016) 125–133.
[23] W. Li, J. Liu, Y. Zhou, S. Wen, Q. Wei, C. Yan, Effect of substrate preheating on the texture, phase and nanohardness of a Ti–45Al–2Cr–5Nb alloy processed by selective laser melting, Scr. Mater. 118 (2016) 13–18.
[24] X.P. Li, J. Van Humbeeck, J.P. Kruth, Selective laser melting of weak-textured commercially pure titanium with high strength and ductility: a study from laser power perspective, Mater. Des. 116 (2017) 352–358.
[25] M. Ghayoor, K. Lee, Y. He, C.-.H. Chang, B.K. Paul, S. Pasebani, Selective laser melting of 304 L stainless steel: role of volumetric energy density on the microstructure, texture and mechanical properties, Addit. Manuf. 32 (2020), 101011.
[26] O. Andreau, I. Koutiri, P. Peyre, J.-.D. Penot, N. Saintier, E. Pessard, Texture control of 316 L parts by modulation of the melt pool morphology in selective laser melting, J. Mater. Process. Technol. 264 (2019) 21–31.
[27] J.J. Marattukalam, D. Karlsson, V. Pacheco, P. Beran, U. Wiklund, U. Jansson, The effect of laser scanning strategies on texture, mechanical properties, and site-specific grain orientation in selective laser melted 316 L SS, Mater. Des. 193 (2020), 108852.
[28] K. Kunze, T. Etter, J. Grässlin, V. Shklover, Texture, anisotropy in microstructure and mechanical properties of IN738LC alloy processed by selective laser melting (SLM), Mater. Sci. Eng. A 620 (2015) 213–222.
[29] T. Bormann, B. Müller, M. Schinhammer, A. Kessler, P. Thalmann, M. de Wild, Microstructure of selective laser melted nickel–titanium, Mater. Charact. 94 (2014) 189–202.
[30] S. Saedi, A.S. Turabi, M.T. Andani, N.S. Moghaddam, M. Elahinia, H.E. Karaca, Texture, aging, and superelasticity of selective laser melting fabricated Ni-rich NiTi alloys, Mater. Sci. Eng. A 686 (2017) 1–10.
[31] S.-.H. Sun, K. Hagihara, T. Nakano, Effect of scanning strategy on texture formation in Ni-25at.%Mo alloys fabricated by selective laser melting, Mater. Des. 140 (2018) 307–316.
[32] H.Y. Wan, Z.J. Zhou, C.P. Li, G.F. Chen, G.P. Zhang, Effect of scanning strategy on grain structure and crystallographic texture of Inconel 718 processed by selective laser melting, J. Mater. Sci. Technol. 34 (2018) 1799–1804.
[33] T.D. McLouth, G.E. Bean, D.B. Witkin, S.D. Sitzman, P.M. Adams, D.N. Patel, The effect of laser focus shift on microstructural variation of Inconel 718 produced by selective laser melting, Mater. Des. 149 (2018) 205–213.
[34] L. Thijs, M.L. Montero Sistiaga, R. Wauthle, Q. Xie, J.-.P. Kruth, J. Van Humbeeck, Strong morphological and crystallographic texture and resulting yield strength anisotropy in selective laser melted tantalum, Acta Mater. 61 (2013) 4657–4668.
[35] C.L. Yang, Z.J. Zhang, S.J. Li, Y.J. Liu, T.B. Sercombe, W.T. Hou, Simultaneous improvement in strength and plasticity of Ti-24Nb-4Zr-8Sn manufactured by selective laser melting, Mater. Des. 157 (2018).
[36] Y.W. Zhang, S.J. Li, E.G. Obbard, H. Wang, S.C. Wang, Y.L. Hao, Elastic properties of Ti–24Nb–4Zr–8Sn single crystals with bcc crystal structure, Acta Mater. 59 (2011) 3081–3090.
[37] P. Priya, B. Mercer, S. Huang, M. Aboukhatwa, L. Yuan, S. Chanudhuri, Towards prediction of microstructure during laser based additive manufacturing process of Co-Cr-Mo powder beds, Mater. Des. 196 (2020).
[38] J. Akram, P. Chalavadi, D. Pal, B. Stucker, Understanding grain evolution in additive manufacturing through modeling, Addit. Manuf. 21 (2018) 255–268.
[39] O. Zinovieva, A. Zinoviev, V. Ploshikhin, Three-dimensional modeling of the microstructure evolution during metal additive manufacturing, Comput. Mater. Sci. 141 (2018) 207–220.
[40] A.R.A. Dezfoli, W.-.S. Hwang, W.-.C. Huang, T.-.W. Tsai, Determination and controlling of grain structure of metals after laser incidence: theoretical approach, Sci. Rep. 7 (2017) 41527.
[41] S. Torquato, Random Heterogeneous Materials Microstructure and Macroscopic Properties, first ed., Springer, New York, 2002.
[42] J. Segurado, R.A. Lebensohn, J.L. Lorca, Chapter One - computational homogenization of polycrystals, Adv. Appl. Mech. 51 (2018) 1–114.
[43] J.P. Kruth, G. Levy, F. Klocke, T.H.C. Childs, Consolidation phenomena in laser and powder-bed based layered manufacturing, CIRP Ann. Manuf. Technol. 56 (2007) 730–759.
[44] A. Halfpenny, Some important practical issues for collection and manipulation of electron backscatter diffraction (EBSD) data from rocks and minerals, J. Virtual Explor. 35 (2010) 1–18.
[45] D.J. Prior, E. Mariani, J. Wheeler, EBSD in the earth sciences: applications, common practice, and challenges, Eds, in: A.J. Schwartz, M. Kumar, B.L. Adams, D. P. Field (Eds.), Electron Backscatter Diffraction in Materials Science, Springer US, Boston, MA, 2009, pp. 345–360.
[46] F. Bachmann, R. Hielscher, H. Schaeben, Texture analysis with MTEX - free and open source software toolbox, Solid State Phenom. 160 (2010) 63–68.
[47] Y.L. Hao, S.J. Li, S.Y. Sun, R. Yang, Effect of Zr and Sn on Young's modulus and superelasticity of Ti–Nb-based alloys, Mater. Sci. Eng. A 441 (2006) 112–118.
[48] R. Yang, Y. Hao, S. Li, Development and application of low-modulus biomedical titanium alloy Ti2448, biomedical engineering, Ed., in: M.A. Laskovski (Ed.), Trends in Materials Science, InTech, 2011.
[49] Y.L. Hao, S.J. Li, S.Y. Sun, C.Y. Zheng, R. Yang, Elastic deformation behaviour of Ti-24Nb-4Zr-7.9Sn for biomedical applications, Acta Biomater. 3 (2007) 277–286.
[50] J. Yvonnet, Computational Homogenization of Heterogeneous Materials With Finite Elements, first ed., Springer, Cham, Switzerland, 2019.
[51] H.-.J. Bunge, Texture Analysis in Materials Science Mathematical Methods, first English ed, Butterworths, London, 1982.
[52] E.J. Garboczi, A.R. Day, An algorithm for computing the effective linear elastic properties of heterogeneous materials: three-dimensional results for composites with equal phase Poisson ratios, J Mech Phys Solids 43 (1995) 1349–1362.
[53] E.J. Garboczi, Finite Element and Finite Difference Programs for Computing the Linear Electric and Elastic Properties of Digital Images of Random Materials, NISTIR, 1998. Technical report 6269Available, http://ciks.cbt.nist.gov/garbocz/manual/man.html.